LAWRENCE
LIVERMORE
NATIONAL
LABORATORY

LLNL-JRNL-485519

The Space-Based Telescopes for Actionable Refinement of Ephemeris Pathfinder Mission

L. Simms, W. De Vries, V. RIot, S. Olivier, A. Pertica, B. Bauman, D. Phillion, S. Nikolaev

June 3, 2011

SPIE Optical Engineering

Disclaimer

Optical Payload for the STARE Pathfinder Mission

Lance M. Simms[a], Willem De Vries[a], Vincent Riot[a], Scot S. Olivier[a], Alex Pertica[a], Brian J. Bauman[a], Don Phillion[a], Sergei Nikolaev[a]

[a]Lawrence Livermore National Laboratory, Livermore, CA, 94550 USA

ABSTRACT

The Space-based Telescopes for Actionable Refinement of Ephemeris (STARE) program will collect the information needed to help satellite operators avoid collisions in space by using a network of nano-satellites to determine more accurate trajectories for selected space objects orbiting the Earth. In the first phase of the STARE program, two pathfinder cube-satellites (CubeSats) equipped with an optical imaging payload are being developed and deployed to demonstrate the main elements of the STARE concept. In this paper, we first give an overview of the STARE program. We then describe the details of the optical imaging payload for the STARE pathfinder CubeSats, including the optical design and sensor characterization. Finally, we discuss the track detection algorithm that will be used on the images acquired by the payload.

Keywords: Space Situational Awareness, Satellites, Space Debris, Orbital Refinement

1. INTRODUCTION

Space is becoming an increasingly crowded place. The Space Surveillance Network (SSN), operated by the United States Air Force (USAF), currently tracks over 20,000 man-made objects larger than ∼10 cm in orbit around the Earth, and the NASA Debris Office estimates that as many as 300,000 objects larger than 1 cm are present in low Earth orbit (LEO) alone.[1] Each year, several satellites typically disintegrate spontaneously into many pieces, further fueling the space debris population. As the Cosmos-Iridium collision of February 2009 proved, the consequences of this overcrowding can be both disastrous and expensive. Worse still, some experts predict that these incidents could cascade and render entire orbital regimes unsafe for satellites.[2]

A principal reason that the USAF tracks space objects is to warn satellite operators when they may need to maneuver their satellites to prevent a collision with another space object. However, the level of positional accuracy maintained by the SSN for the complete set of tracked space objects is insufficient to predict collisions with an adequate degree of certainty, and multiple false alarms occur daily as a result. Because of the high false alarm rate - approximately one per month for the average, active satellite, or approximately ten thousand false alarms per expected collision - satellite operators typically choose not to maneuver their satellites based on these warnings. This is where the STARE program comes in.

The objective of the STARE program is to collect the information necessary to provide satellite operators with actionable collision warnings. What is needed is improved accuracy in the knowledge of orbital trajectories for those space objects that are predicted to pass close to an active satellite. For instance, an accuracy of 100 meters in these orbital trajectories at the time of closest approach would reduce the collision false alarm rate to approximately one per decade for the average, active satellite, or about one hundred false alarms per expected collision. This lower collision false alarm rate, and the corresponding higher likelihood of collision for each warning, would enable satellite operators to respond effectively by repositioning satellites (approximately once during the lifetime of the typical satellite) to avoid potential collisions.

The question then becomes how to reach the necessary level of accuracy in the knowledge of these orbital trajectories. A detailed architecture study performed at Lawrence Livermore National Laboratory using a sophisticated high-performance computer modeling and simulation environment for Space Situational Awareness (SSA) has recently concluded that a network of approximately a dozen small, inexpensive, space-based, optical imaging sensors can be used to achieve the accuracy needed to provide actionable satellite collision warnings to all maneuverable satellites in low Earth orbit (LEO).[3,4]

To demonstrate the essential elements of the STARE concept, the initial phase of this program involves the development and deployment of two pathfinder nano-satellites. These satellites will use a standard cube-satellite

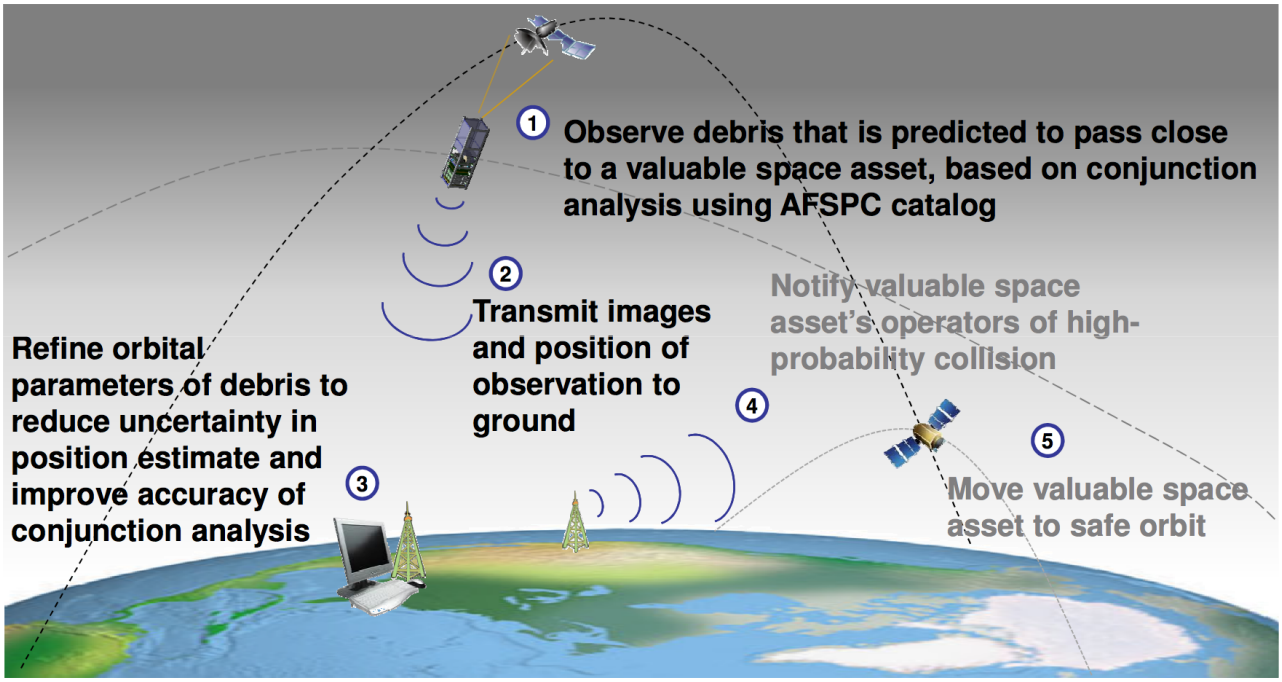

Figure 1. A high-level diagram illustrating the STARE concept. In the pathfinder mission, steps 1-3 will be executed for verification that the orbits of the chosen targets are indeed refined. In the full constellation, steps 4-5 will allow satellite owners to move their assets if a collision is deemed probable.

(or CubeSat) format, and will be launched into a low earth orbit (most likely a 480×780 km orbit with an inclination of 60°) where they will be used to image space objects at optical wavelengths. The images will be processed, along with Global Positioning Service (GPS) data, to refine the trajectory of the targets. The latter process is highlighted in circles 1-3 of Figure 1. If successful, the mission will pave the way for a small constellation of similar satellites capable of refining ephemerides for all of the satellites and debris pieces in LEO involved in close approaches. The nano-sats will provide actionable information, allowing satellite owners to move their assets as in circles 4-5.

It is beyond the scope of this paper to address all the details (target selection, ground communication, etc.) of the STARE pathfinder mission. Nevertheless, we will attempt to motivate the mission in Section 2 and provide a sufficient overview of it in Section 3. The rest of the paper is devoted to the optical payload and the acquisition and processing of track data. In Section 4 we describe the optics and imager implemented in the payload, and in Section 5 we present the algorithm used to detect stars and satellite tracks in the target images.

2. MOTIVATION FOR THE STARE MISSION

There are several reasons why a space-based observing platform is preferable for orbital refinement. For instance, loss of observing time due to cloud coverage is not an issue and neither is image degradation from atmospheric turbulence. And mobile telescopes inherently have better sky coverage than their fixed, ground-based partners. However, the most important reason is observing efficiency.

Due to the fact that LEO satellites maintain such a close proximity to earth, a typical fixed observatory is only able to observe them for less than two hours after sunset and before dawn. And that is just for satellites that pass overhead. In contrast, an orbiting satellite in a 90 minute orbit is able to see a very large fraction of the full LEO population many times a day.

The latter point is made more concrete in Figure 2, which compares the observing efficiency of hypothetical ground-based and spaced-based networks of orbital refinement telescopes. The spaced-based networks, shown in dark and light blue, consist of a series of nano-sats arranged in three separate planes (either 6 or 8 per plane,

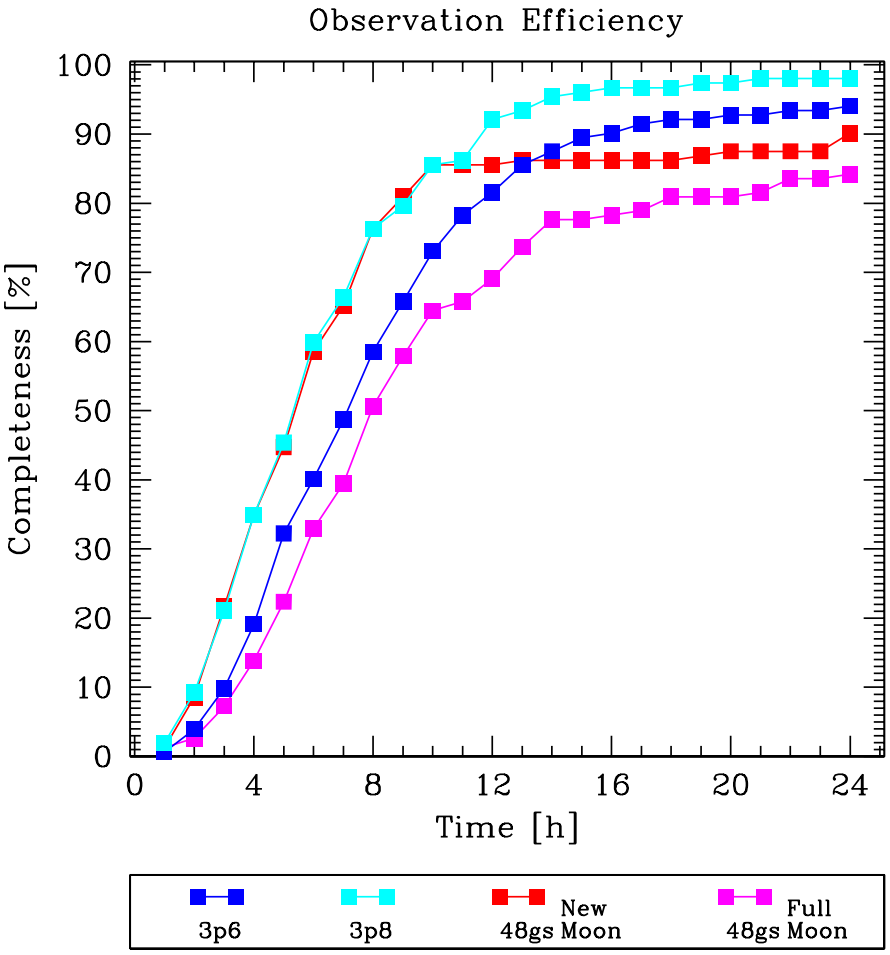

Figure 2. A plot showing the superior observing efficiency of a space-based constellation of telescopes over a ground-based one. Each point shows the percentage of 760 total observations (152 LEO targets; 5 observations per target) that each telescope network has made after the time shown on the x-axis. The dark and light blue symbols show the efficiency for a series of space-based telescopes arranged in 3 planes (6 and 8 per plane, respectively). The red and pink symbols show the results for a network of 48 ground-based 0.5m telescopes equipped with low read-noise detectors spread evenly around the globe in longitude and between $-45°$ and $+45°$ in latitude. The red symbols show a scenario during New Moon and pink shows the same scenario during Full Moon. Targets are assumed to be 1m diameter spheres in the case of a satellite and 10cm in the case of debris.

respectively). Each nano-sat is equipped with an 8cm telescope and a detector with moderate read noise. The ground-based network consists of 48 telescopes spread out more or less evenly across the globe in longitude, with the latitude varying between -45° and +45°. The telescopes were allowed to be placed at a location regardless of whether there was solid ground there, and no obstruction due to cloud cover was considered, making it a highly idealized scenario. Each of them has a diameter of 0.5m and is assumed to have state-of-the-art detector having only a few electrons read noise. Distinction is also made between the period around the full moon (pink curve), where observing time is more limited than the period around the new moon (red curve).

The plot in Figure 2 shows the completeness fraction for a set of 152 targets that need to be observed. A total of five observations per target are required, making the total amount of observations 760. The target positions are based on real catalog entries and an observation date of August 16, 2010. One can see that the 3 plane-8 satellites per plane arrangement reaches about 80% efficiency in 8 hours. While the idealized ground-based network has similar performance during these first 10 hours, it lags behind noticeably during the remainder of time. This is because the observation locations are fixed. They cannot reach the remaining targets, and so level out before reaching 90%. The spaced-based system, on the other hand is able to reach these targets and make virtually all the required observations during the 24 hour period.

The spaced-based network, with its smaller telescopes and mediocre detectors is thus able to out-perform an idealized set of large telescopes with low-noise detectors on the ground. This is the primary motivation for the STARE constellation.

3. STARE PATHFINDER MISSION OVERVIEW

3.1 STARE Pathfinder Mission Goals

The primary objective of the STARE pathfinder mission is to demonstrate the feasibility of using nano-satellites to refine the orbital parameters of selected space objects to a level of accuracy that is useful for providing actionable collision warnings to satellite operators. As discussed in Section 1, it can be shown that 100 meters is a useful level of positional accuracy for the orbital trajectories of space objects that are predicted to pass close to an active satellite. We have therefore adopted this value as the goal for the refined orbital positional accuracy of space objects observed by the STARE pathfinder CubeSats.

Table 1 presents some other technical goals for the STARE pathfinder mission. Operational goals for the pathfinder mission, which we expect to launch in summer of 2012, include achieving a mission lifetime of at least one month and completing observations of at least 30 space objects.

Performance		Stretch Goal	Usefulness Level
Orbital Accuracy After Refinement		≤ 50 m ≥ 1 day ahead	< 100 m ≥ 1 day ahead
Characteristics of Objects	Range	< 1000 km	< 100 m
	Size	< 0.1 m^2	< 1m^2
	Tangential Velocity	< 10 km/s	< 3 km/s
	Spectrum	Sunlight	Sunlight

Table 1. A list of the goals for the STARE pathfinder mission. The second row refers to the minimum limit at which accuracy can be considered valid.

3.2 Choice of Orbital Regime

One of the primary constraints on the STARE mission is the size of the satellites themselves. The 3U CubeSat limits the diameter of our primary optic to less than 10 cm, which, along with the characteristics of the sensor limits the maximum distance and relative velocity of the targets we are trying to image. With the pathfinder Cypress IBIS-5B CMOS sensor, we are limited to distances of about 100 km and relative velocities of 3 km/s. For the full STARE constellation, a better sensor choice will allow distances on the order of 1000 km and relative velocities as high as 7 km/s*.

Based on signal to noise calculations with these considerations in place, we have simulated an orbital platform for the pathfinder satellites to maximize the number of observation opportunities,[4] with the following criteria constituting a valid observation (i.e. one capable of reducing the size of the uncertainty ellipsoid of the target to the desired level):

- A maximum separation smaller than 100 km
- A relative tangential velocity less than 3 km/s
- A solar separation angle larger than 30 degrees (i.e., a solar exclusion angle of 30 degrees)
- An Earth exclusion angle of 85 degrees
- A lunar exclusion angle of 1 degree

*Scheduling for the full STARE constellation will take into account everything that factors into the calculation of target signal-to-noise: distance, size, relative velocity, solar illumination, and observation geometry. As such, the CubeSat is not strictly limited to a fixed distance or relative velocity.

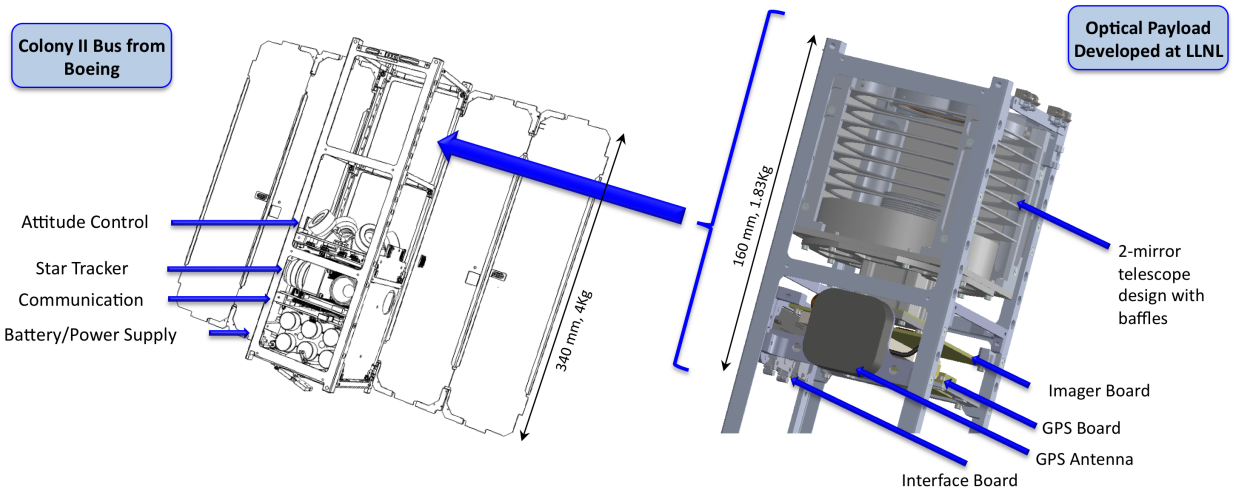

Figure 3. The Colony II Bus, shown on the left, is the backbone of the STARE Satellite. The bus communicates with the Optical Payload, shown on the right, via an RS-422 connection.

These criteria, along with considerations of downlink opportunities, solar panel orientation and attitude control, drag-limited orbital lifetime, and GPS signal coverage, limit the number of useful orbital regimes for the STARE pathfinder satellites.

Examining the close conjunctions from the simulations occurring over a one-week period with the cataloged objects in LEO shows that a 700 km polar orbit with an inclination of about 90 degrees is optimal for the STARE constellation. In particular, a sun-synchronous orbit of 98 degrees simplifies satellite attitude control with respect to solar panel power generation. The orbits of the STARE pathfinder satellites will differ slightly from this optimum. While not yet precisely known, they are scheduled to have a perigee near 480 km, an apogee near 780 km, and an inclination of about 60°.

3.3 The STARE Satellite

As shown in Figure 3, the 3U STARE CubeSats consist of two main components: a Colony II Bus supplied by Boeing and an optical payload developed at LLNL. The actual integration and testing of the payloads and buses will take place at two different institutions: the Naval Postgraduate School (NPS) and Texas A&M.

The Colony II Bus is essentially the brain of the satellite. It handles communication with the ground, controls the solar panels, distributes power to the various components, and provides attitude control with an on-board star tracker/reaction wheel system. It also contains a non-volatile flash filesystem consisting of two SD cards, one being the RAID mirror of the other, that we will use to store our images and telemetry data. Proper functioning of the bus, particularly in the attitude control system, is critical to success of the mission.

Connected to the Bus with an RS-422 link is the optical payload. The payload contains the optical elements, the visible CMOS imager and its carrier board, an OEMV-1G GPS receiver and antenna, and several additional interface components. A dedicated Marvell PXA 270 microprocessor in the payload handles communication with the Colony II Bus and orchestrates the image acquisition and processing along with retrieval of concurrent GPS data. Further discussion of the optical payload can be found in Section 4.

3.4 Observing Strategy

At the time of writing, the STARE pathfinder mission only plans on having one dedicated ground station for communication with the satellites. This station, located at NPS, will allow for about 2 minutes of data transfer per day at 9600 baud. We are thus limited to downloading about 1Mb of data per day, which is close to the size of our 1280×1024 images.

Fortunately, the vast majority of the 1,310,720 pixels in an image will contain only detector noise and sky background, so they are of no use to us.[†] The information we are actually after is the following:

1. **Precise position and time of satellite at time of observation**
   This information is contained in the GPS logs that are recorded simultaneously with the image capture. Each GPS log is approximately 200-300 bytes.

2. **Stellar Positions (in detector coordinates)**
   The positions of the stars will give us a very accurate pointing of the satellite once matched up to cataloged stellar positions. We will record the location and flux of the 100 brightest stars in the image.

3. **Track Endpoint Positions (in detector coordinates)**
   Along with the timing and angular information from the two items above, the track endpoints tell us exactly where the satellite was at the start and end of the observation (in the transverse plane).

While we will have the capability to download a full, raw image from the payload to the ground (a typical image averages 600-700 kB in size once compressed) for diagnostic and calibration purposes, the three pieces of information above are what we will be routinely receiving on the ground. The GPS data will be logged from the on-board receiver and the star and track data will be extracted from the images by using the algorithm described in Section 5, which will run in the PXA 270 payload microprocessor.

Of course, this all relies on the assumption that our images contain a track and a suitable number of stars to yield an astrometric solution. To ensure this is the case, we will command the satellite to point toward a given target (when it is passing through a field with an ample number of bright stars) and begin acquiring images at the calculated time of conjunction. In a typical observing sequence, ten consecutive one-second exposures will be taken along with their corresponding time-stamps. The ten image allotment should guarantee that one or two images[‡] contain the track even with the 1000 m uncertainty of its orbital elements.

4. OPTICAL PAYLOAD

Although the optical payload contains many components, the heart of it is comprised of a reflective Cassegrain telescope and a CMOS imager at its focus. Each will be discussed in turn.

4.1 The Telescope

A wide field of view is obviously beneficial for our application since it 1) increases the chance that we will capture the entire streak in one exposure and 2) increases the maximum velocity the target can have relative to our satellite. To obtain a wide field with minimal aberrations in the small 10×10×10 cm space offered in the CubeSat payload is a challenge, though.

The telescope, shown in Figure 4, is a Cassegrain design, which can be optionally modified with corrective lenses near the focal plane. The lenses will help to reduce abberations at the field edges. The telescope delivers an approximately f/2.5 beam, and with our 8.6 mm × 6.9 mm imager, this equates to a field of view of about 2.08°×1.67°. Other details of the telescope are provided in the caption of Figure 4, and the expected performance will be discussed in the next section.

Another challenge of the optical system is that there is no focusing mechanism (at least for the pathfinder mission). Thermal expansion and contraction in the space environment are thus of great concern. The telescope is designed to have a depth of focus of 10 microns and an Invar support structure will be used to provide stiffness under changing temperatures. Preliminary thermal calculations show that focus will be maintained over the -20 to +60°C range expected in our orbit.

[†]It should be emphasized that we will not be *tracking* the targets. Rather, we will stare at the fixed stars and wait for the target to pass through the field of view. The stars will then appear as point sources in the image and the track will be an extended object. With a 4" aperture and 1 s exposure, we will not see objects beyond 12^{th} magnitude.

[‡]It is preferable to have the entire streak and both track endpoints recorded in one image. However, refinement is still possible if two segments of the streak are captured in two separate images (i.e. one image showing a segment of the satellite entering the detector and the other image showing a segment leaving the detector).

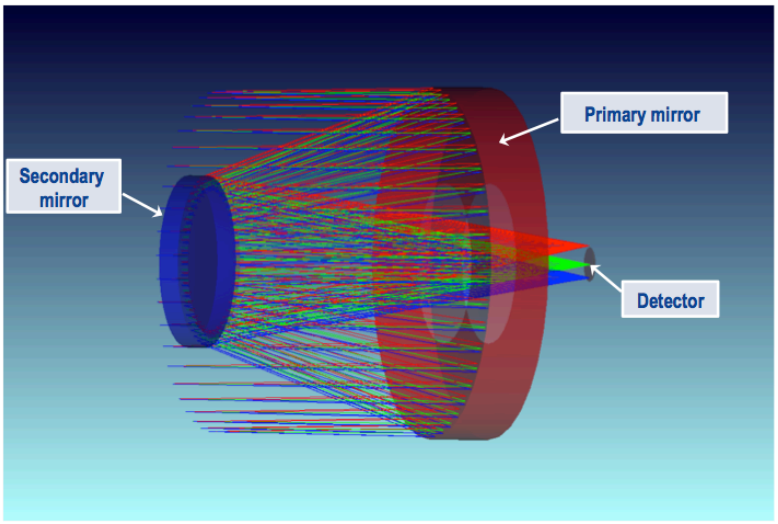

Figure 4. The Cassegrain optical system employed in the STARE telescope. The telescope consists of two reflective conics. Optionally, a set of corrector lenses may be placed near the detector to reduce aberrations at the field edges. With a 225 mm focal length and 85 mm aperture, the system will yield a resolution of about 29 μrad/pixel across the Field of View, which corresponds to 6.1″/pixel. At a range of 100 km, this is about 2.9 m/pixel. The entire field size is 2.08°×1.67°. A baffling system, not shown in the figure, will reduce stray light.

4.2 The Imager

After collecting the star and track light, the telescope will focus it onto a Cypress IBIS5-B-1300 CMOS imager.[5] This sensor, which has a 1280×1024 format with 6.7 micron pixels, is mainly intended for video rate imaging. We are choosing to use the IBIS5-B-1300 because Boeing is able to provide it in a fully integrated system (which includes the PXA 270 microprocessor) that will facilitate communications with the Colony II Bus and save us a great deal of development time and expenses, allowing us to finish these pathfinder satellites in time for launch. In the full constellation of refinement satellites, we most certainly intend to use a low noise, high performance imager, which the Cypress IBIS5-B-1300 is not. With that being said, we have to validate that the sensor is able do its job.

We have tested the IBIS5-B-1300 extensively in the laboratory to verify that it will meet our mission requirements. The characteristics we measured for the sensor, along with the ones specified by Cypress, are shown in Table 2. One will note that there is a very large discrepancy between the two sets of measurements, particularly in the noise. This is likely due to the fact that our measurements used the on-board 10 bit A/D converter of the chip. Cypress confirms that the A/D converter has an extensive number of missing bit codes in the 1024 possible digital values, and it can be shown that this greatly magnifies the measured noise of the analog signal.

The values in Table 2 can be used to predict the signal to noise delivered by the optical system for a range of

Imager Parameter	LLNL Measured Value	Cypress Specification
Fixed Pattern Noise	$< 0.20\%$	$< 0.80\%$
Well Depth	$< 62{,}500$ e$^-$	70,000 e$^-$
Linearity	INL < 3 LSB	INL < 10 LSB
Dark Current	1233 e$^-$/s/pix	410 e$^-$/s/pi
Dark Current Non-Uniformity	510 e$^-$/s	400 e$^-$/s
Read Noise (Spatial)	150-260$^-$	40 e$^-$
Read Noise (Temporal)	147 e^-	40 e$^-$
Dynamic Range	256:1 (48 dB)	1563:1 (64 dB)
Bad Pixel Percentage	$< 0.005\%$	

Table 2. Characterization of the Cypress IBIS5-B-1300 imager.

scenarios we might encounter.[4] As a specific case, we consider a spherical piece of debris with a radius of r=0.3 m and a reflectivity of 50% (albedo of 0.5). The object produces Lambertian scattering of the incident V-band portion of sunlight. A range of relative velocities are considered, these determining the dwell time per pixel and the number of photoelectrons received by a given pixel along the track. For the detector, we assume a quantum efficiency (QE)/fill factor product of 0.22 photoelectrons/photon. The outcomes of the various scenarios are shown in Table 3.

The numbers shown indicate that we can achieve the mission goals. With the track recognition algorithm presented in Section 5, we can tolerate a SNR as low as 2.5 and still refine orbits. The noise due to the missing bit codes is by far the most concerning. It greatly limits the number of objects that we can work with. The good news is that the noise is very uniform over the detector, as shown in Figure 5, and the percentage of bad pixels is extremely low. We can thus use tracks without concern for where they are located on the detector.

Again, it is important to note that this imager is only being implemented to show that the orbital refinement scheme provided by nano-satellites works. Once the methods are proven, we will choose an imager that has lower read noise and dark current, better QE and fill factor, etc. for the nano-sat constellation. This will vastly open up the list of potential targets.

5. ON-BOARD STAR AND TRACK RECOGNITION

5.1 Satellite Recognition and Endpoint Determination

The issue of autonomously detecting satellite and airplane tracks in images is by no means a new one. For decades, these tracks have been nothing more than a nuisance for astronomers–foreground artifacts that must be removed in the preprocessing of data–and several methods for getting rid of them have been discussed in the literature. For instance, the RAST algorithm[6] removes satellite streaks using a geometric approach that assumes the tracks are straight lines and Storkey et al.[7] use the RANSAC algorithm to allow for removal of curved tracks and scratches as well.

Neither of the these methods are concerned with accurately determining where the track starts and ends in the image, however. Levesque presents an algorithm for accurate endpoint detection from ground-based images, but this again relies on the track being straight.[8] Since the attitude of the STARE satellites will not be precisely controlled, the telescope may be rotating about the pointing axis, which could potentially produce tracks with a large and unknown curvature. We therefore require a novel algorithm that can deliver sub-pixel endpoint determination for tracks with arbitrary curvature. It should be emphasized that the algorithm is not concerned with detection of faint streaks, but rather high fidelity endpoint determination for streaks with ample SNR.

To avoid confusion while describing the algorithm in this section, we will reserve the term *satellite* for our STARE CubeSat. The debris or satellite we are trying to image will be referred to as the *target*.

Target	Relative Velocity (km/s)	Dwell Time/Pixel (ms)	Streak Length (Pixels)	Electrons/Pixel	SNR
100 km	1	2.98	336	2227	10.8
	3	0.99	1008	742	3.7
	5	0.62	1679	445	2.2
	7	0.43	2351	318	1.6
	9	0.35	3022	247	1.2
250 km	1	7.44	134	891	4.4
	3	2.48	403	297	1.5

Table 3. Signal to Noise Ratio (SNR) for the r=0.3 m target objects described in the text. The average value of the read noise, RN=200 e− was used to calculate the noise. Sky background noise and dark current shot noise are negligible. The calculation assumes the telescope is not drifting or rotating, an issue that will be touched upon in Section 5.

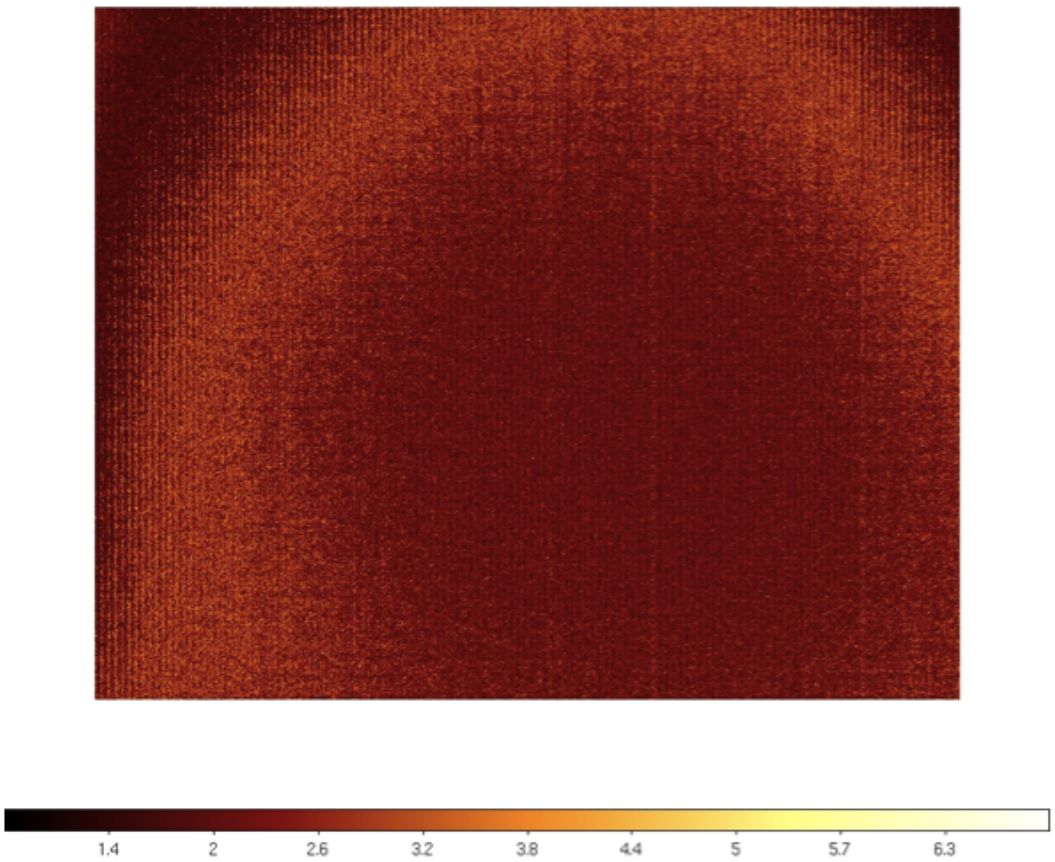

Figure 5. Temporal Noise Map of the IBIS5-B-1300. The map was obtained by taking the standard deviation across 40 dark images. The color bar shows the noise in ADU and the conversion gain is about 61e−/ADU.

5.1.1 Target Tracks in STARE Images

During a STARE observation, the satellite will stare at a fixed star background and allow the target to streak across the field of view. Changes in the orientation of the satellite during the observation are unwanted since they could potentially reduce the dwell time per pixel of the stars and the target (the exception being the case where the motion of the satellite causes inadvertent rate tracking of the target). But rotation of the satellite about the two axes perpendicular to the telescope pointing is of less concern because it simply adds to the transverse velocity component of the target and causes the stars to streak in a uniform manner across the detector.[§] It will not produce curvature in the streak left by the target.

Rotation about the pointing axis, on the other hand, could potentially induce significant curvature. If the satellite has a rotational velocity of $\dot{\theta}$ about the pointing axis, which we call z, and the target has velocity components (v_x, v_y, v_z) and coordinates of

$$x = x_o + v_x t, \qquad y = y_o + v_y t, \qquad z = z_o + v_z t, \tag{1}$$

with respect to the satellite center of mass, then the location of the target in the detector coordinate system is

[§]Note that we are simplifying by approximating the path of the target as a straight line during the exposure, which it is not.

given by

$$x' = (x'_o + v'_x t)\cos(\dot{\theta}t) + (y'_o + v'_y t)\sin(\dot{\theta}t), \qquad y' = -(x'_o + v'_x t)\sin(\dot{\theta}t) + (y'_o + v'_y t)\cos(\dot{\theta}t), \tag{2}$$

where the primes represent the mapping of object space to pixel space and rotation of the satellite about the x and y axis has been folded into the components v_x and v_y.

One can gain an appreciation for the form of Equation 2 by considering that for the case of $x_o = y_o = 0$, it is the parametric representation of a spiral. We do not anticipate angular velocities of the telescope above $0.1°$/s, so a spiral pattern should never be observed in our images. But $\dot{\theta} = 0.1°$/s is enough to make a Hough Transform ineffective for basic detection and create an error as large as two pixels for a track that extends all the way across the image if a global linear fit is used.

Fortunately, we are not interested in fitting the entire track. As long as we know $\dot{\theta_x}$, $\dot{\theta_y}$, and $\dot{\theta_z}$ reasonably well[¶], the track endpoints (x'_o, y'_o), (y'_f, y'_f) are sufficient to refine the orbit of the target. The primary intent of the STARE algorithm is to find these coordinates.

5.2 STARE Endpoint Determination Algorithm

The following subsections follow the numbering in Figure 6, which gives an overview of the STARE algorithm.

5.2.1 Image Correction

Before we begin identifying the stars and tracks in our images, we must first clean them. Because our algorithm identifies stars and tracks as a contiguous set of pixels above a noise threshold, T, pre-processing of the data is crucial to its success. The basic steps of the image correction, shown in box **1** of Figure 6, are as follows:

1. **Sky Image Subtraction**
   The 10 raw images acquired during an observation sequence will be slightly offset from each other so that a given pixel sees sky background most of the time. A median filter is used on these 10 images to produce a sky image. Subtracting this sky image from a raw image very accurately removes both dark current and sky background.

2. **Bad Pixel Masking and Interpolation**
   Bad pixels are problematic for thresholding. These pixels can easily be mapped during routine calibration of the detector and stored as a mask in non-volatile memory. They are first zeroed in each of the background subtracted images and then corrected with a nearest neighbor filter that uses the local values and gradients across the pixel to fill in a reasonable value.

3. **Low Pass Filter**
   The corrected image is optionally smoothed using a Gaussian kernel with a FWHM on the order of 1-2 pixels. The smoothing helps ensure that tracks are contiguous. If the bad pixel density becomes excessive, the kernel can be extended at the expense of increasing the error in endpoint estimation.

5.2.2 Object Detection

After the image is corrected, it is searched for contiguous sets of pixels that have a value above T. This step is shown in box **2** of Figure 6. With both real and simulated images, typically $T = 3.5 \cdot RN$, where RN is the read noise of the detector, produces good results. The read noise will dominate both the sky noise and dark current shot noise with our one second integration times.

Once a contiguous set of pixels has been identified, it is characterized as a star, track, or unknown object (such as a delta or Compton scattered worm) based upon its ellipticity (e) and the number of pixels (N) it contains. Using a cut of $e > 0.8$ and $N > 20$ should effectively identify all real tracks. A perfectly straight track should have $e = 1$; the margin $e = 0.8 - 1.0$ allows for curvature and the possibility of overlapping stars or cosmic rays. The chance of a muon hit producing a track greater than 20 pixels long is extremely low.

[¶]We should have this information from calibration data taken before the observation.

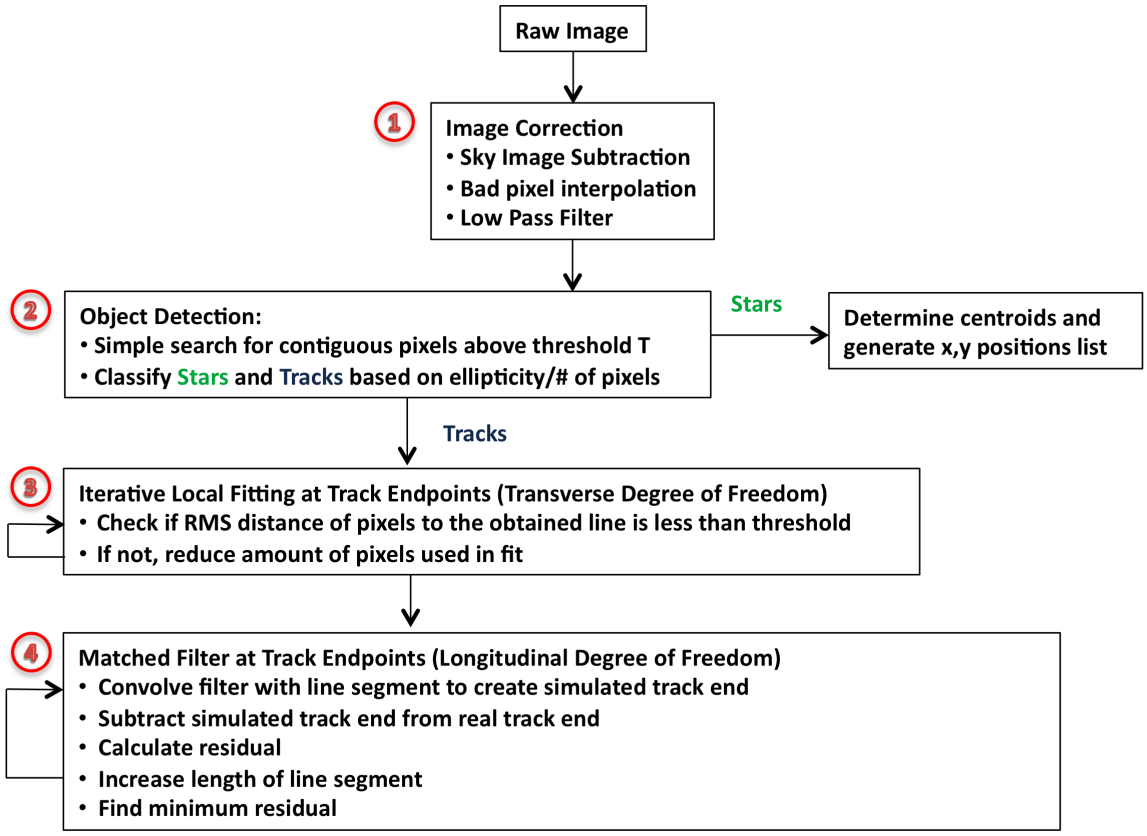

Figure 6. Flow diagram for the various steps used in the STARE endpoint detection algorithm.

Confusion of cosmic rays and stars is more troublesome. Because our optical system produces a sub-pixel point spread function (PSF), most stars will actually appear as 1-4 pixel points rather than the nice gaussian profiles encountered in astronomy applications. Based on previous space-based measurements, though, we do not anticipate a significant amount of 1-4 pixel cosmic ray events in our one second exposures.[9,10] At geomagnetic latitudes below 50°, we expect about 0.706 events per exposure, and above 50° we may see up to 12. With these rates we will still be able to obtain an astrometric solution from the list of star centroids even with the contamination.

5.2.3 Iterative Local Fitting at Track Endpoints (Transverse Degree of Freedom)

The next step, step **3**, is to find the endpoints for each of the tracks identified in step **2** above. As previously mentioned, applying a global linear fit to the track to find its endpoints may result in large errors. But a local linear fit to the track at each endpoint can still help in constraining their possible locations. The question we are then met with is how many pixels to use in the fit. If two many are used, the curvature of the track will force the slope toward the global average. If too few are used, the estimate is vulnerable to detector noise, bad pixels, etc.

We might consider using the second derivative as a criterion:

$$\frac{d^2y'}{dx'^2} = \frac{2\dot{\theta}(-v'_x\sin(\dot{\theta}t) + v'_y\cos(\dot{\theta}t)) - \dot{\theta}^2((x'_o + v'_x t)\cos(\dot{\theta}t) + (y'_o + v'_y t)\sin(\dot{\theta}t))}{2\dot{\theta}(-v'_x\cos(\dot{\theta}t) - v'_y\sin(\dot{\theta}t)) - \dot{\theta}^2((x'_o + v'_x t)\sin(\dot{\theta}t) + (y'_o + v'_y t)\cos(\dot{\theta}t))} \tag{3}$$

(note that we have ignored the any change in the angular velocity, $\ddot{\theta} = 0$). But this expression requires accurate knowledge of x'_o, y'_o, v'_x, and v'_y, which we will not have.

Our solution to the problem is to use an iterative weighted least squares fit to each track endpoint until the root mean square deviation of distance from the included track pixels to the line is below a certain threshold, σ_D^{max}. Starting with all $N_{pix} = N$ pixels identified in the track, we fit a line using the expression:

$$m = \frac{\sum_{i=0}^{N_{pix}} x'^2 \sum_{i=0}^{N_{pix}} Iy' - \sum_{i=0}^{N_{pix}} Ix' \sum_{i=0}^{N_{pix}} Ix'y'}{N_{pix} \sum_{i=0}^{N_{pix}} Ix'^2 - \left(\sum_{i=0}^{N_{pix}} Ix'\right)^2}, \qquad b = \frac{N_{pix} \sum_{i=0}^{N_{pix}} Ix'y' - \sum_{i=0}^{N_{pix}} Ix' \sum_{i=0}^{N_{pix}} Iy'}{N_{pix} \sum_{i=0}^{N_{pix}} Ix'^2 - \left(\sum_{i=0}^{N_{pix}} Ix'\right)^2}, \tag{4}$$

where I is the pixel intensity and the indices on x', y', and I have been left out for notational convenience. Then we calculate the distance of the track points to the line using

$$D = \frac{I\left(mx' - y' + b\right)}{I_{max}\sqrt{m^2 + 1^2}}, \tag{5}$$

where I_{max} is the maximum pixel intensity for the N_{pix} pixels used in the fit. If the RMS of this value, σ_D, is below the threshold σ_D^{max} then we consider the fit valid. If not, we remove n pixels from the end of the track opposite to the one we are trying to fit and repeat the above procedure. Thus, at the j^{th} iteration, we will be fitting with $N_{pix} = N - n * j$ pixels. We also incorporate a minimum of $N_{pix} = N_{min}$ pixels to be used in the fit, a value that will be based upon the calibration data we obtain during the mission.

The threshold σ_D^{max} and whether we use the intensity weighting in Equation 5 will depend on the actual PSF of our system. Figure 7 shows results for a simulated track where $\dot{\theta} = 1.0°/s$ and $\sigma_D^{max} = 0.50$ was used without weighted fitting. The eventual error in endpoint estimation was less than 0.1 pixels in both x and y.

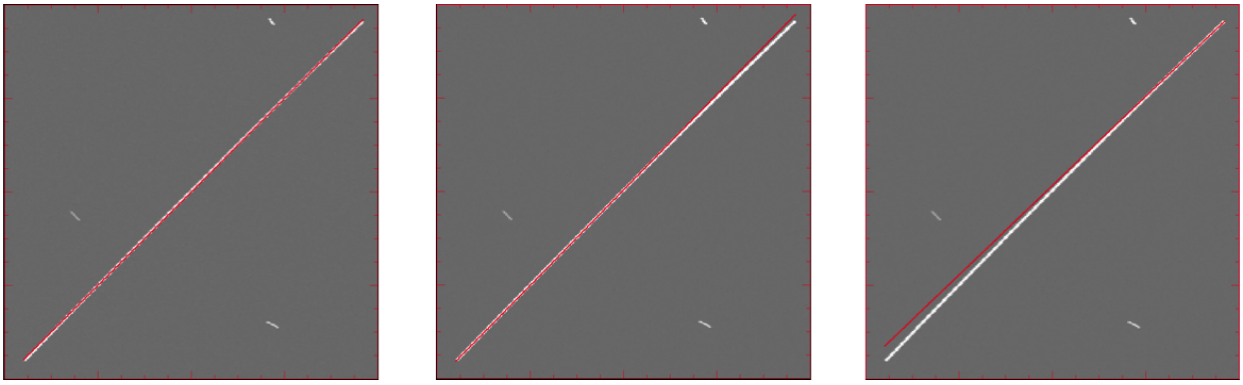

Figure 7. An example of the local fitting at each endpoint. The left image shows the track fit in red when all pixels were used, the middle when the left 200 pixels were used, and the right when the right 170 pixels were used.

5.2.4 Matched Filter at Track Endpoints (Longitudinal Degree of Freedom)

Once the track has been fit at each endpoint, we have a good approximation of the path the target took along the detector near that point. What is left is to determine precisely where the target was along this path at the start (or end) of the exposure (step **4**). Simply recording the first or last pixel with a value above T will obviously result in errors. Accurately determining the location of the target requires that we take into account the PSF of the optical system and the kernel used in the low pass filter of step **1**.

To do this, we first consider a Region Of Interest (ROI) around the roughly estimated endpoint that spans $R \times R$ pixels. An example ROI with $R = 7$ is shown in the upper left image of Figure 8. Our goal is to reproduce this ROI with a simulated one obtained by convolving a line segment with a filter that matches the PSF and

kernel described above. The form of the line segment is already known from the fit we obtained in step **3**. The length of it will tell us exactly where the endpoint is located.

After dividing each simulated pixel into r subpixels, we start at the edge of the simulated ROI from which the track emerges and create a line segment of length $L = 1/r$. The segment is convolved with the filter to produce a track in the simulated ROI, as shown in the bottom left image of Figure 8. We subtract the simulated ROI from the real one and square the residual. We then increase the length of the line segment by $1/r$ and repeat the process so that after $R \cdot r$ iterations, we will have a set of $R \cdot r$ residuals. The minimum of these tells us where the endpoint is.

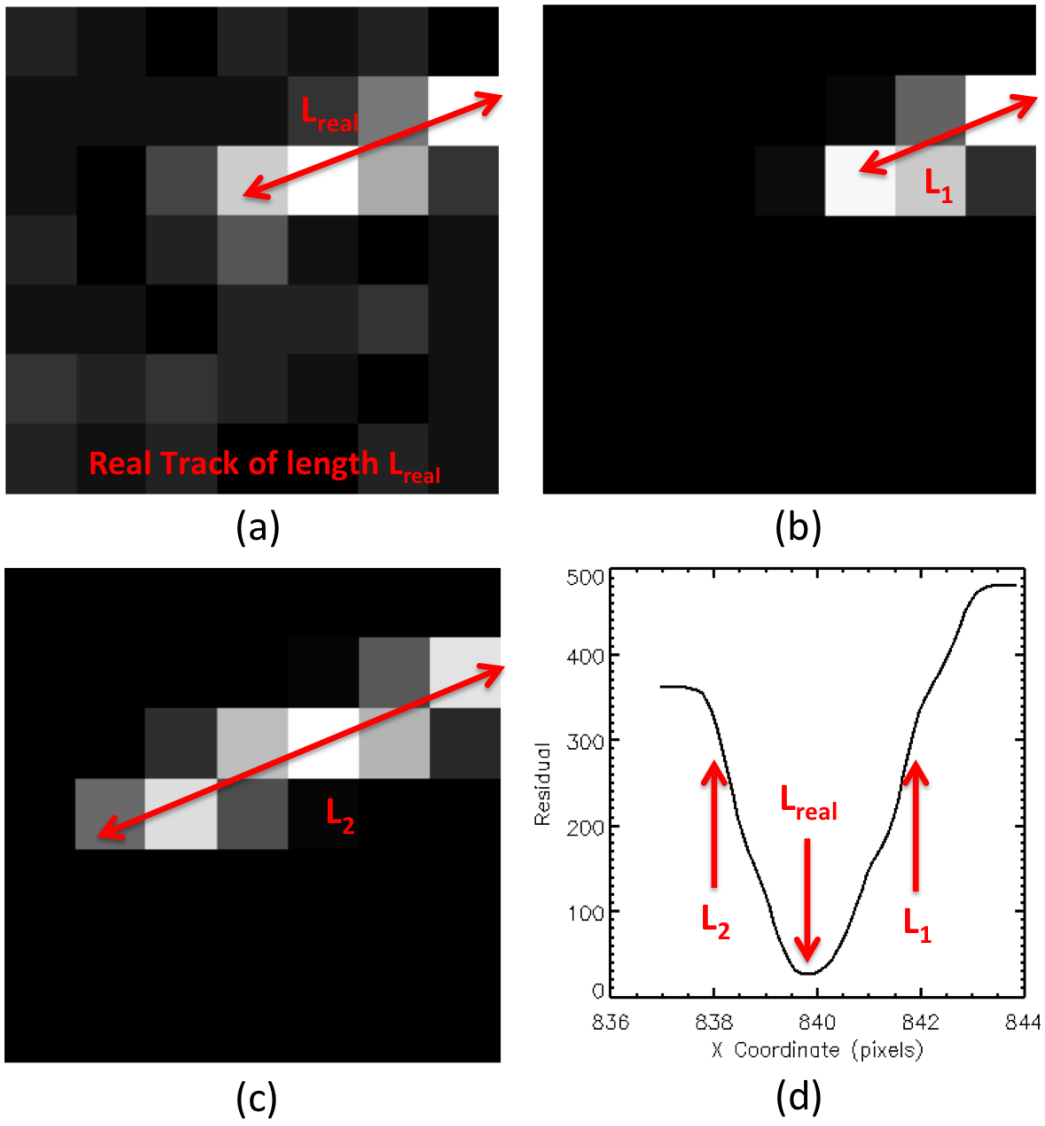

Figure 8. Illustration of the matched filter process. (a) shows an ROI taken from a corrected raw image. (b) shows a simulated ROI, where a line segment of length L_1 has been convolved with a match filter to attempt to reproduce the real track in (a). In (c) the length has been extended to L_2 as part of the iterative process. And in (d), the entire simulated ROI has been spanned to produce a residual at all $R \cdot r$ grid points. The first and last 10 points appear flat because the edges of the ROI are ignored due to convolution edge effects. The real track length L_{real} is evident at the minimum of the residual curve.

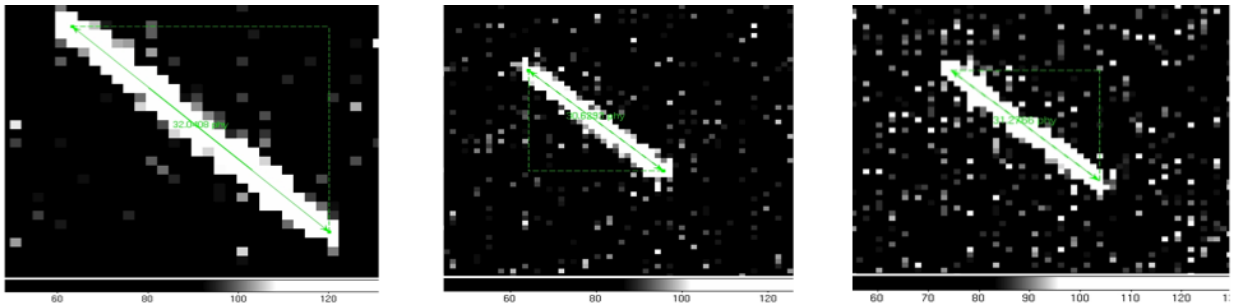

Figure 9. Endpoint determination for satellite track detected in three separate Oceanit images. While precise endpoint coordinates are not available for comparison as they are in the simulated images, the reported endpoints match up well with what we expect based on the PSF of the system.

5.3 Results for Simulated and Real Images

The results from testing the STARE algorithm on real images obtained by ground-based telescopes are encouraging. For these images, we were not able to generate a median sky frame or obtain a bad pixel map, but subtraction of the mode sufficed for image correction. In Figure 9, we show tracks found in three separate Oceanit images after running them through the algorithm. The ends of the green line segment indicate where the extracted endpoints are located. Although there are no official coordinates for these reported in the Oceanit data, inspection by eye shows that they line up well with the locations expected from the 1.9 pixel FWHM PSF.

We have also done extensive testing on simulated tracks and star fields. This is useful because we can compare the measured endpoint to the true endpoint and determine the accuracy of the algorithm as a function of track length, orientation, brightness, etc. It also allows us to find bugs that might cause a crash in the optical firmware such as improper handling of tracks that extend all the way to the edge of the frame.

To comprehensively measure the error in the estimated endpoints, we did a 10 hour run in which 400 images were generated and analyzed. Real star fields were sampled and then tracks with random orientation and length were generated in a number of different brightness intervals. As a proxy for brightness, we chose to use the quantity of *photons per micron*, which is the x-axis of Figure 10. The reason for this is that a track of a given

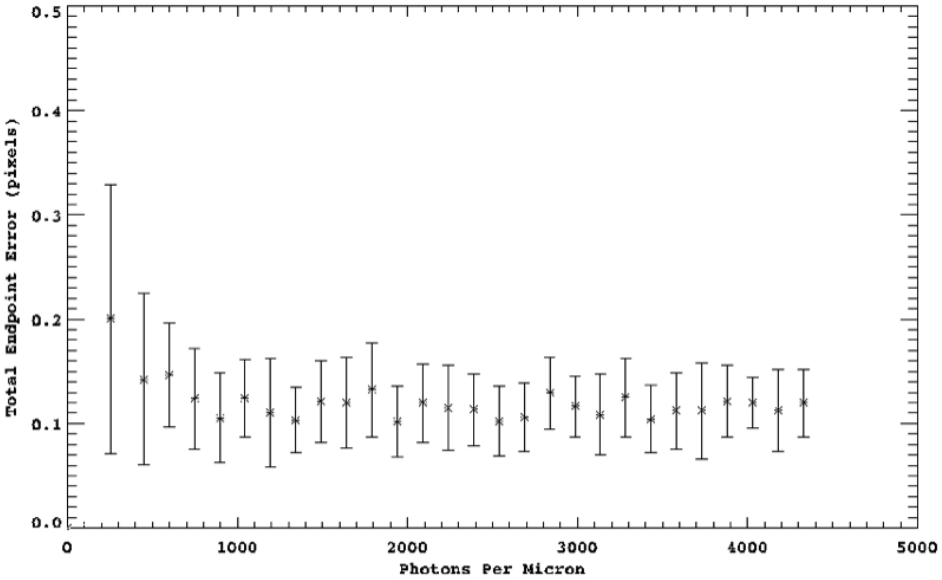

Figure 10. A plot showing the total endpoint error from a run of 400 tracks of random lengths, orientation, and brightness. The y-axis shows the total endpoint error and the x-axis shows photons per micron, both of which are described in the text. At 250 photons per micron, the SNR ranges from 2-4. At 600 photons per micron, the SNR ranges roughly from 6-12. These values depend on the orientation of the track relative to pixel boundaries.

brightness will produce varying signal to noise ratios depending on how it is oriented relative to the detector. For instance, if a track is centered over the boundary between a row of pixels, it will produce roughly half the SNR as it would when centered directly over one of the two rows.

On the y-axis of Figure 10 is the total error in the endpoint estimate, $Err = \sqrt{x_{err}^2 + y_{err}^2}$, where x_{err} and y_{err} are simply the difference between the real and measured coordinates. The plot shows that at a level of about 600 photons per micron, the error approaches a near constant value of $Err = 0.14$. This is expected from the choice of $r = 10$ for the simulated grid, which should produce an error of roughly 0.1 pixels for each coordinate (the step in length at each iteration is $L = 0.1$ pixels). The value of 600 photons per micron corresponds to a SNR in the range of 6-12, depending on the track orientation. One can see that at a value of 250 photons per micron, which is roughly a SNR of 2-4, the error is slightly larger. But it is still sub-pixel and not prohibitive for the purpose of orbital refinement.

Of course, these are highly idealized numbers. Aside from a neglect for errors in GPS measurements, timing, and attitude control, the simulations ignore the low fill factor of the CMOS detector we are using for the pathfinder mission. Because the pixel is not sensitive over its entire area, we lose information every time the target spot passes over the pixel boundaries. Although proper intrapixel laboratory measurements of the Cypress IBIS5 have not been performed, we can expect anywhere from 0.3-0.7 pixel errors due to the device alone. These errors are still tolerable for orbital refinement of large, close objects, though. And the future constellation of satellites will most definitely use detectors with a fill factor near unity to take advantage of the accuracy of this algorithm.

6. CONCLUSION

The STARE pathfinder mission will pave the way for a constellation of satellites that will provide refined orbital information for satellites and debris in orbit around earth. These "space traffic cams" will drastically lower the number of false collision warnings, allowing satellite operators to take action when their assets are in danger. In addition to describing the motivation for the future STARE constellation in this paper, we have presented the goals of the STARE pathfinder mission and how we will meet them. We have also provided an overview of the optics and detector that will be used in our CubeSat based prototypes, as well as the algorithm that will extract the target track endpoints and star positions from the images they acquire.

REFERENCES

1. Committee on Space Debris, [*Orbital Debris: A Technical Assessment*], National Academy Press, Washington D. C. (1995).
2. Kessler, D. J. and Cour-Palais, B. G., "Collision frequency of artificial satellites: The creation of a debris belt," *Journal of Geophysical Research* **83**, 2637–2646 (jun 1978).
3. Phillion, D., Pertica, A., Fasenfest, B., Horsley, M., Vries, W. D., Springer, H. K., Jefferson, D., Olivier, S., Hill, K., and Sabol, C., "Large-scale simulation of a process for catalouging small orbital debris," *Proceedings of the Advanced Maui Optical and Space Surveillance Technologies Conference* (September 14-17, 2010).
4. De Vries, W., "Collision avoidance through orbital refinement using imaging from a constellation of nanosatellites," In Print (2011).
5. Cypress Semiconductor Corporation, *IBIS5-B-1300 CYII5FM1300AB 1.3 MP CMOS Image Sensor Manual.* 198 Champion Court, San Jose, CA (August 2007). Document Number: 38-05710 Rev. *C.
6. Ali, H., Lampert, C., and Breuel, T., "Satellite tracks removal in astronomical images," in [*Progress in Pattern Recognition, Image Analysis and Applications*], *Lecture Notes in Computer Science* **4225**, 892–901, Springer Berlin / Heidelberg (2006).
7. Storkey, A. J., Hambly, N. C., Williams, C. K. I., and Mann, R. G., "Cleaning sky survey data bases using hough transform and renewal string approaches," *Monthly Notices of the Royal Astronomical Society* **347**, 36–51 (jan 2004).
8. Levesque, M., "Automatic reacquisition of satellite positions by detecting their expected streaks in astronomical images," *Advanced Maui Optical and Space Surveillance Technologies Conference* (2009).
9. Shaw, D. and Hodge, P., "Cosmic ray rejection in STIS CCD images," tech. rep. (jun 1998).
10. AMS Collaboration, "Protons in near earth orbit," *Physics Letters B* **472**, 215–226 (jan 2000).

Prepared by LLNL under Contract DE-AC52-07NA27344